Exchange bias effect in Au-Fe$_3$O$_4$ dumbbell nanoparticles induced by the charge transfer from gold

Mikhail Feygenson,[1,*] John C. Bauer,[2] Zheng Gai,[3] Carlos Marques,[4] Meigan C. Aronson,[4,5] Xiaowei Teng,[6] Dong Su,[7]
Vesna Stanic,[8] Volker S. Urban,[9] Kevin A. Beyer,[10] and Sheng Dai[2]

[1]*Chemical and Engineering Materials Division, Spallation Neutron Source, Oak Ridge National Laboratory,
Oak Ridge, Tennessee 37831, USA*
[2]*Chemical Sciences Division, Oak Ridge National Laboratory, Oak Ridge, Tennessee 37831, USA*
[3]*Center for Nanophase Materials Sciences, Oak Ridge National Laboratory, Oak Ridge, Tennessee 37831, USA*
[4]*Department of Physics and Astronomy, Stony Brook University, Stony Brook, New York 11794, USA*
[5]*Condensed Matter Physics and Materials Science Department, Brookhaven National Laboratory, Upton, New York 11973-5000, USA*
[6]*Department of Chemical Engineering, University of New Hampshire, Durham, New Hampshire 03824, USA*
[7]*Center for Functional Nanomaterials, Brookhaven National Laboratory, Upton, New York 11973, USA*
[8]*Photon Sciences Directorate, Brookhaven National Laboratory, Upton, New York, 11973, USA*
[9]*Biology and Soft Matter Division, Oak Ridge National Laboratory, Oak Ridge, Tennessee 37831-6475, USA*
[10]*X-ray Science Division, Argonne National Laboratory, Argonne, Illinois 60439, USA*

We have studied the origin of the exchange bias effect in the Au-Fe$_3$O$_4$ dumbbell nanoparticles in two samples with different sizes of the Au seed nanoparticles (4.1 and 2.7 nm) and same size of Fe$_3$O$_4$ nanoparticles (9.8 nm). The magnetization, small-angle neutron-scattering, synchrotron x-ray diffraction, and scanning transmission electron microscope measurements determined the antiferromagnetic FeO wüstite phase within Fe$_3$O$_4$ nanoparticles, originating at the interface with the Au nanoparticles. The interface between antiferromagnetic FeO and ferrimagnetic Fe$_3$O$_4$ is giving rise to the exchange bias effect. The strength of the exchange bias fields depends on the interfacial area and lattice mismatch between both phases. We propose that the charge transfer from the Au nanoparticles is responsible for a partial reduction of the Fe$_3$O$_4$ into the FeO phase at the interface with Au nanoparticles. The Au-O bonds are formed, presumably across the interface to accommodate an excess of oxygen released during the reduction of magnetite.

I. INTRODUCTION

In recent years, Au-Fe$_3$O$_4$ dumbbell nanoparticles have been widely studied because of their applications in magnetic resonance imaging [1–3], hyperthermia treatment [4], drug delivery [5], DNA-based biosensors [6], and catalysis [7,8]. The most intriguing property of Au-Fe$_3$O$_4$ dumbbell nanoparticles is the exchange bias (EB) effect reported by several groups [9–11]. When a ferromagnet is in close proximity to an antiferromagnet, the direct exchange interaction between the moments in each can create an unidirectional anisotropy which impedes the reversal of the ferromagnetic moment. The magnetization loop is subsequently shifted along the field axis by the exchange bias field (H_{EB}). The EB effect is well understood in thin films, but it is a more complex phenomenon in magnetic nanoparticles. The size of nanoparticles, their crystallinity, and their oxidation state can greatly affect the strength of H_{EB} in nanoparticles. Previous experiments on Co-core/CoO-shell nanoparticles found that H_{EB} depends on a net magnetic moment at the core-shell interface induced by lattice strain between the Co core and CoO shell [12]. The variation of this moment with the strain is ultimately responsible for the nonmonotonic dependence of H_{EB} on Co-core thickness, in contrast to Co/CoO thin films, where the same dependence is inversely linear. A core-shell interface is not the only prerequisite for the EB in magnetic nanoparticles.

For example, in single-component NiO nanoparticles, the presence of uncompensated magnetic sublattices led to the horizontal shift of the magnetization loop, reminiscent of the EB [13]. Considering that the magnetic and structural properties of Fe$_3$O$_4$ and Au nanoparticles are greatly modified from their bulk counterparts [14–17], there are several possible explanations for the origin of the EB effect in the dumbbell nanoparticles. The bulk Fe$_3$O$_4$ is a ferrimagnetic (FiM) material with inverse spinel structure and lattice constant which is almost double (8.396 Å) that of gold (4.083 Å). The bulk gold is weakly diamagnetic; however, 1.5 nm Au nanoparticles can sustain localized magnetic moments and show a ferromagneticlike behavior when capped with the thiol-ligand shell, due to 5d localized holes generated by the charge transfer from Au to S [18]. Thus, ferromagnetic/ferrimagnetic coupling between Au and Fe$_3$O$_4$ nanoparticles can lead to the EB, similar to Fe-core/γ-Fe$_2$O$_3$-shell nanoparticles [19]. The magnetic structure of 9 nm Fe$_3$O$_4$ nanoparticles was found to be nonuniform and consist of magnetically ordered core and surface shell of canted spins [15]. The number of canted spins is presumably increased at the Au/Fe$_3$O$_4$ interface in the dumbbell nanoparticles [9]. The coupling between the ordered core and canted shell can lead to the EB, as well, and it was observed for single-component NiFe$_2$O$_4$ and γ-Fe$_2$O$_3$ nanoparticles [19,20]. A similar explanation is based on the exchange coupling between antiphase boundaries (APBs) with canted spins and FiM regions within Fe$_3$O$_4$ nanoparticles. The APBs were experimentally observed in magnetite thin films grown on MgO substrate, which has a cubic structure

---

*feygensonm@ornl.gov

similar to Au [21,22]. Finally, the exchange bias might arise from exchange interactions between ferrimagnetic Fe_3O_4 and antiferromagnetic FeO phases. The FeO phase can originate at the Au/Fe_3O_4 interface due to the charge transfer from gold which reduces Fe_3O_4 into FeO. This explanation was first suggested by Pineider *et al.* [23] to explain the exchange bias effect in Au/iron-oxide core-shell nanoparticles.

The EB effect in the $Au-Fe_3O_4$ dumbbell nanoparticles depends on sample preparation and measurements details. When the reaction solvent is slightly polarized, multiple nucleation sites on the surface of Au seed nanoparticles become available for Fe_3O_4, resulting in flowerlike structures [11]. The flowerlike structures show significantly larger exchange bias fields compared to dumbbells [10]. In the powder form, the blocking temperature of the $Au-Fe_3O_4$ dumbbell nanoparticles is increased due to interparticle interactions [11,24]. Moreover, close packing of nanoparticles can lead to the EB effect due to partial restoration of the bulklike magnetic properties, reported in Co/CoO nanoparticles [25].

In order to understand the origin of the EB effect in a complex system such as $Au-Fe_3O_4$ dumbbell nanoparticles, it is crucial to obtain the experimental data on particle dimensions, crystallinity, and possible interparticle interactions. Because we are interested in the length scales ranging from interatomic distances of a few angstroms to extended structures of tens of nanometers, several experimental techniques have to be combined. Experimental studies of a crystal structure of nanoparticles have always been a challenge. Conventional Rietveld refinements of the powder-diffraction data often fail to provide an adequate picture of the crystal structure of nanoparticles. Small size, defects, and lack of translational symmetry in nanoparticles result in broad and overlapping Bragg peaks. Often, crucial information about local crystal structure is hindered in diffuse scattering, which is orders of magnitude lower than Bragg-peak intensities and ignored during Rietveld analysis. The pair-distribution function (PDF) analysis of diffraction data has been successfully applied to address this challenge. In PDF analysis, both diffuse and Bragg scattering are analyzed simultaneously, thus providing insights into crystal structure and disorder in nanoparticles.

In this work, we present a study of two $Au-Fe_3O_4$ dumbbell nanoparticles with the same sizes ($R = 9.8$ nm) of Fe_3O_4 nanoparticles, but different sizes of Au seed nanoparticles. These are 4.1 and 2.7 nm for the samples Au-4 and Au-3, respectively (see Table I). We will use a combination of

magnetization, transmission microscopy, small-angle neutron and x-ray scattering measurements to accurately determine the Au and Fe_3O_4 nanoparticle dimensions, and demonstrate that interparticle interactions play no appreciable role in the exchange bias effect. Magnetization and synchrotron x-ray diffraction measurements confirm that the antiferromagnetic FeO phase forms within the Fe_3O_4 nanoparticle, presumably at the Au/Fe_3O_4 interface. The exchange bias occurs as a result of the coupling between antiferromagnetic FeO and ferrimagnetic Fe_3O_4 phases. By appealing to x-ray absorption spectroscopy experiments carried out on similar samples [26,27] and to PDF analysis of diffraction data, we argue that the FeO phase is induced by the charge transfer from Au nanoparticles. The relation between H_{EB} and the crystal structure of Au and Fe_3O_4 nanoparticles is also discussed.

II. SAMPLES AND EXPERIMENTS

Monodisperse Au seed nanoparticles were first synthesized using a procedure developed by Sun *et al.* [28,29]. $HAuCl_4 \cdot 3H_2O$ (200 mg, 0.5 mmol) was dissolved in a solution of tetralin (20 mL) and oleylamine (20 mL) by stirring under N_2 atmosphere at $0°$ or $20°$ C to obtain a particle size near $R = 4$ and 3 nm, respectively. Then a reducing solution, made by dissolving tert-butylamine-borane complex (88 mg, 1.0 mmol) in 2 mL of tetralin and 2 mL of oleylamine by sonication, was rapidly injected into the Au solution. The solution changed from an orange color to brown and then gradually into red. The product was diluted in ethanol and collected by centrifuging at 8000 rpm for 10 min.

To synthesize $Au-Fe_3O_4$ dumbbell nanoparticles, a procedure described in [30] was used and is briefly outlined. The reaction began by stirring a solution of 1 ml oleic acid (3 mmol) in 20 ml 1-octadecene under a flow of N_2 at $120°$ C for 20 min. Then 0.3 mL of $Fe(CO)_5$ (2 mmol) was injected into the solution under N_2 atmosphere and stirred for 5 min. 0.5 ml of oleylamine was injected into the mixture, followed by an appropriate volume of the Au nanoparticle solution to equal approximately 20 mg. The solution was heated to reflux ($\sim$310 °C) for 45 min. After the reaction cooled down to room temperature, the solution was diluted in ethanol and centrifuged at 7500 rpms for 10 min and redispersed into hexane or d-toluene prior to magnetization and scattering measurements.

The dc magnetization measurements were carried out using a Quantum Design Magnetic Property Measurement System (MPMS). For the measurements, 10 μL of the original aliquots were dispersed in 50 μL of liquid paraffin and then injected into a standard gelatin capsule to reduce interparticle interactions. The gelatin capsules were fastened in plastic straws for immersion into the magnetometer. In order to measure the exchange bias field, a sample is cooled from 300 K to a target temperature in an applied magnetic field of 50 kOe. The magnetization is then measured as a function of an applied magnetic field. The exchange bias field is calculated as $H_{EB} = |H_{c1} - H_{c2}|/2$, where H_{c1} and H_{c2} are the negative and positive coercive fields, respectively. The standard field-cooled (FC) and zero-field-cooled (ZFC) measurements of temperature-dependent magnetization were used to define the

TABLE I. Size and size distribution of the dumbbell samples obtained by TEM, SANS, and SAXS measurements. H_{EB} is the exchange bias field at 2 K. Size of nanoparticles is in nanometers (nm) and exchange bias field is in Oersted (Oe).

Sample	Au-4		Au-3	
	Fe_3O_4	Au	Fe_3O_4	Au
R_{TEM} (nm)	7.8 ± 1.2	4.1 ± 1.7	7.8 ± 1.4	2.7 ± 0.6
R_{SANS} (nm)			8.5 ± 1.5	2.3 ± 0.3
R_{SAXS} (nm)	9.3 ± 1.2	3.8 ± 0.4	9.8 ± 1.2	2.8 ± 0.7
H_{EB} (Oe)	1919(6)		1350(7)	

blocking temperature (T_B). FC and ZFC measurements were carried out in the field of 500 Oe.

The small-angle neutron scattering (SANS) experiments were conducted with the Bio-SANS (CG-3) instrument at the High Flux Isotope Reactor in the Oak Ridge National Laboratory with a neutron wavelength of 6.09 Å [31]. The samples were dispersed in deuterated toluene to reduce incoherent scattering from hydrogen. Sample-to-detector distances of 0.3 and 14 m were used to cover the q range from 0.003 to 0.67 Å^{-1}, where q is the scattering vector defined as $q = 4\pi/\lambda \sin\theta$, and λ and θ are the neutron wavelength and scattering angle, respectively. The data were corrected for the detector sensitivity, sample transmission, and background scattering from d-toluene.

The synchrotron small-angle x-ray scattering (SAXS) measurements were carried out at the beam line X6B at the National Synchrotron Light Source at Brookhaven National Laboratory using x rays with wavelength $\lambda = 1.24$ Å. The X6B beam line was configured for the SAXS experiment with sample-to-detector distance of 120 mm. The magnetic field of 1.2 Tesla was applied perpendicular to the incoming beam. The samples were in the original solution. The data was corrected for the beam attenuation, dark current, and background scattering from solution. The SANS and SAXS data were analyzed using software from the NIST Center for Neutron Research [32].

The synchrotron x-ray pair distribution function (PDF) measurements were carried out at the beam lines 11-ID-B ($\lambda = 0.2127$ Å) and 6-ID-C ($\lambda = 0.12488$ Å) at the Advanced Photon Source, Argonne National Laboratory. The dried powders were measured in a 0.5 mm kapton capillary. The standard Ni bulk was measured to estimate the resolution of each instrument. The measurements were carried out at room temperature in ambient conditions. The sample Au-3 was measured at 11-ID-B with a short detector-to-sample distance (D) of 110 mm. We had only 4 mg of the sample available, thus using shorter D allowed us to gain more intensity. In contrast, we used the high-q-resolution configuration ($D = 240.5$ mm) to measure the Au-4 sample at 6-ID-C. The bulk Au and mixture of Fe$_3$O$_4$ and α-Fe$_2$O$_3$ bulk powders were measured under the same experiential conditions as a reference. The PDF data were analyzed using the PDFgui program [33].

III. RESULTS

Transmission electron microscopy (TEM) measurements of the as-synthesized Au-4 sample [Fig. 1(a)] show a large population of dumbbell nanoparticles, with darker contrast indicating Au and lighter one indicating Fe$_3$O$_4$ nanoparticles. Both particles appear to be nearly spherical and fairly monodisperse. Analysis of TEM images reveals the average radius of 4.1 ± 1.7 and 7.8 ± 1.2 nm for Au and Fe$_3$O$_4$ nanoparticles, respectively [Fig. 1(b)]. The electron diffraction rings of a single dumbbell nanoparticle [Fig. 1(c)] are well indexed with two phases: face-centered-cubic (fcc) Au and inverse spinel structure of Fe$_3$O$_4$. We find that free Fe$_3$O$_4$ nanoparticles are present in the sample because some Fe atoms did not precipitate onto Au nanoparticles and self-reduced into free iron nanoparticles, which were later oxidized into magnetite. Some of the particles appear to have a "flowerlike" morphology, presumably due to the coalescence of individual magnetite nanoparticles. Such variations in the particle's shape are undesirable because it complicates the modeling of small-angle and PDF data. Moreover, the agglomeration of magnetic nanoparticles leads to the formation of a disordered interface which can induce the exchange bias. The centrifugation of nanoparticles and their dispersion in paraffin were employed to reduce the shape effects on the scattering data modeling and exchange bias, respectively.

We compare magnetic properties of the sample Au-4 with the reference sample, consisting of the mixture of single-component Au and Fe$_3$O$_4$ nanoparticles with similar sizes (Fig. 2). The ZFC magnetization of the dumbbell nanoparticles is steadily increasing from 2 up to 190 K, where the sharp upturn is observed. The upturn corresponds to the antiferromagnetic (AFM) phase transition at the Néel temperature $T_N = 190$ K of FeO, previously reported in FeO/Fe$_3$O$_4$ core-shell nanoparticles [34–36]. These results provide limited evidence that the FeO phase is antiferromagnetically ordered below 190 K, although temperature-dependent neutron-diffraction measurements are required to unambiguously determine its magnetic state. Above $T_B \sim 200$ K, ZFC magnetization is merged with the FC magnetization. The blocking temperature of magnetic nanoparticles is related to the energy barrier $\triangle E$ separating two preferred directions of magnetization via Arrhenius's law $T_B \approx \triangle E/k_b$, where k_b is the Boltzmann
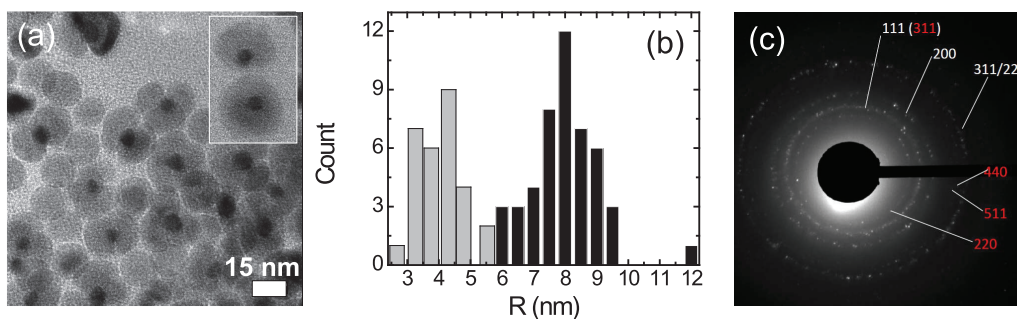

FIG. 1. (Color online) (a) A representative TEM image of the sample Au-4. The darker contrast indicates Au nanoparticles and the lighter one indicates Fe$_3$O$_4$ nanoparticles. Inset: confirms a dumbbell shape of nanoparticles. (b) The size distribution of Fe$_3$O$_4$ (black bars) and Au (gray bars) nanoparticles, obtained from analysis of several TEM images. (c) The electron-diffraction pattern of a single nanoparticle in the sample Au-4. The red numbers indicate to Fe$_3$O$_4$ spinel structure reflections; white numbers are reflections corresponding to the Au face-centered-cubic structure.
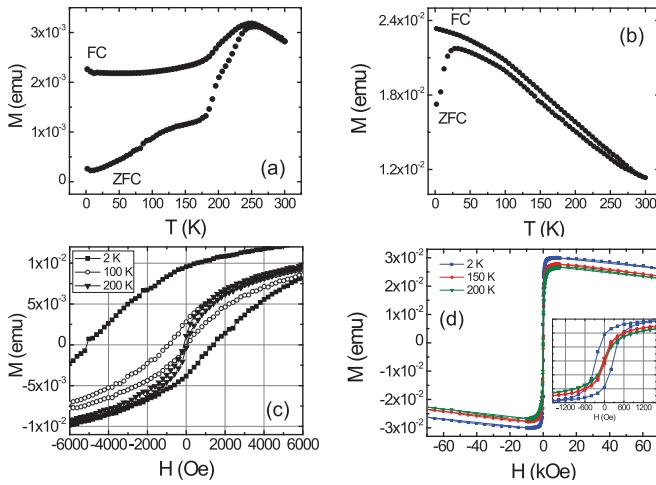
FIG. 2. (Color online) Temperature-dependent ZFC and FC magnetizations for (a) Au-4 sample and (b) free solution of Fe_3O_4 and Au nanoparticles. The field-dependent magnetization measured after field cooling in 50 kOe from 300 K for (c) Au-4 and (d) reference samples at various temperatures. Inset: the same plot at lower fields, showing no horizontal shift of the hysteresis loop.

FIG. 3. The exchange bias field H_{EB} as a function of temperature for Au-4 (■), Au-3 (●), and aged Au-3 (▲) samples. Solid lines are guides for the eye.

constant [37]. If dipolar interparticle interactions are present, then $\triangle E = KV + E_{int}$, where K is the magnetocrystalline anisotropy constant, V is the particle magnetic volume, and E_{int} is the energy of interactions [38,39]. In our previous work, we demonstrated that dilution in paraffin weakens the dipolar interactions of Co/CoO nanoparticles to the extent that no measurable effect on the blocking temperature was detected [12]. Thus, we conclude that increase of T_B in the dumbbell nanoparticles is due to the exchange biasing, as previously reported for the magnetic core-shell nanoparticles [12,23,34,35]. The mixture of Fe_3O_4 and Au nanoparticles shows two blocking temperatures, $T_{B1} = 25$ K and $T_{B2} = 283$ K [Fig. 2(b)], with no indications of the AFM transition at 190 K. Using $K = 1.35 \times 10^5$ erg/cm^3 for the bulk magnetite [14] and assuming no interactions, we estimated the radius of the magnetite nanoparticles to be 5.5 and 12.2 nm, respectively. Our estimations are approximate, since the enhancement of the effective magnetic anisotropy from its bulk value was observed in iron-oxide nanoparticles [14,40,41]. The latter is smaller than the radius of Fe_3O_4 nanoparticles obtained with TEM because magnetic volume is reduced due to the shell of canted spins [15,42,43]. The former corresponds to the larger agglomerates of Fe_3O_4 nanoparticles, occasionally observed with TEM in the free magnetite nanoparticles sample. It is worth noting that ZFC $M(T)$ changes the slope at ~100 K in both dumbbell samples [Figs. 2(a) and 7(a)] and the reference sample [Fig. 2(b)]. We attribute this change to the Verwey transition, which is observed at substantially reduced temperature relative to that of bulk magnetite, which is 120 K [44]. The reduction of Verwey temperature and broadening of ZFC magnetization around the transition are consistent with the previous magnetization measurements of magnetite nanoparticles [14,45,46].

In order to further investigate the origin of T_B enhancement in the dumbbell nanoparticles, we carried out field-dependent magnetization loop measurements. Figure 2(c) shows the
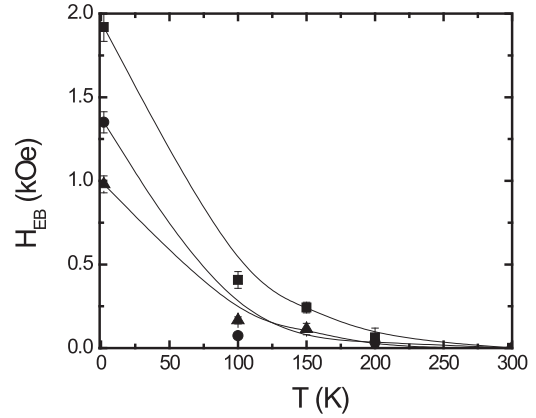
magnetization loop $M(H)$ of the sample Au-4, after cooling from room temperature in a field of 50 kOe to various target temperatures. The dumbbell nanoparticles show a substantial shift of the loop towards negative fields. The loop shift is due to the exchange bias, which is likely due to exchange coupling of the ferrimagnetic Fe_3O_4 with antiferromagnetic FeO phase, evident in $M(T)$ measurements. The maximum exchange bias field of 1919 Oe at 2 K was observed for the sample Au-4, while it is significantly lower (1350 Oe) in the sample Au-3. We see that H_{EB} first becomes nonzero at $T_B \sim 200$ K in each dumbbell sample and increases with decreasing temperature (Fig. 3). In contrast, H_{EB} remains zero at all temperatures for the solution of single-component Au and Fe_3O_4 nanoparticles under the same experimental conditions. The absence of the loop shift is in agreement with $M(T)$ measurements, which showed no indication of the FeO phase. We note that in our dumbbell nanoparticles, the T_B appears to be slightly higher than T_N. Although the exchange bias effect was reported for the samples with $T_B > T_N$ [47], neutron-diffraction measurements are required for determining the T_N of our nanoparticles [48].

The combination of SANS and SAXS experiments is used to provide independent measurements of the dumbbell nanoparticle dimensions and to probe possible interparticle interactions. Neutrons are sensitive to the light elements, and hence ligand-coated dumbbell nanoparticles provide a sharp core-shell contrast for neutrons [inset of Fig. 4(a)]. X rays are more sensitive to heavy elements and simpler core contrast for the dumbbell nanoparticles is realized [inset of Fig. 4(c)]. Our TEM studies indicated that the dumbbell sample consists of epitaxially linked polydisperse Au and Fe_3O_4 nanoparticles coated with OA/olyemine ligands. Lacking a scattering form factor to describe such system, we first studied the as-synthesized dumbbell sample Au-3 after refluxing. At this stage, the sample contains a dispersion of seed Au nanoparticles and slowly nucleating Fe_3O_4 nanoparticles. An analysis of this sample will provide us with dimensions of Au nanoparticles in the dumbbell sample. We then fix them during refinement of the dumbbell sample, which will make it more reliable. The nucleation has completed after 12 hours, which is significantly slower that the averaged SANS measurement
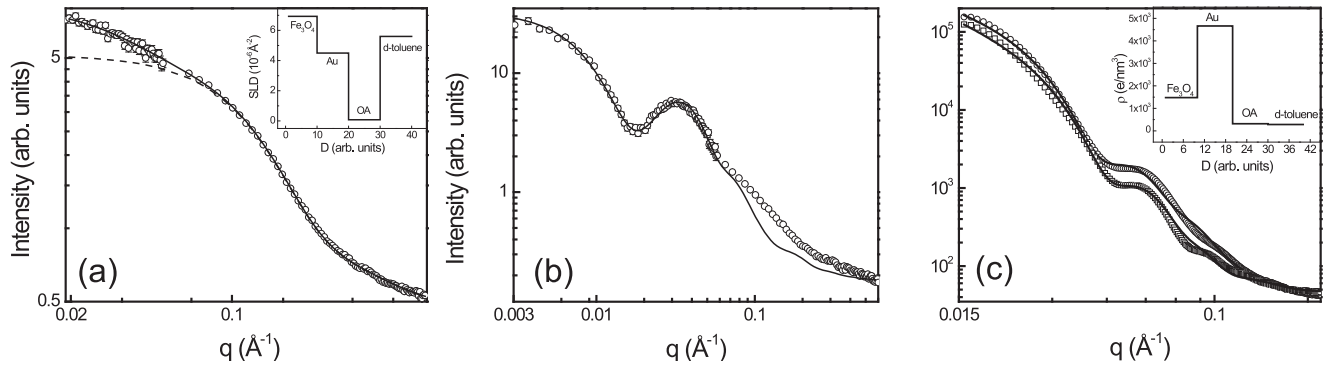
FIG. 4. (a) SANS data at 300 K (open circles) for the as-synthesized Au-3 sample. The solid line is the fit to the model of spheres with bimodal Schulz size distribution. Dotted line is the model with the polydisperse Au nanoparticles only. (b) SANS data for the same sample after 12 hours. The solid line is the best fit with two fractal models. (c) SAXS data for both Au-3 (○) and Au-4 (□) samples. Solid lines are the fits to the model of two fractals with polydisperse spheres. Insets in (a) and (c) are the scattering length density (SLD) and electron density (ϱ) profiles, respectively.

time of two hours. The SANS intensity for the as-synthesized Au-3 sample is plotted as a function of the scattering vector q in Fig. 4(a). The q dependence of the SANS intensity is fitted using a sum of two form factors. The first form factor describes spherical Au-core/OA-shell nanoparticles assuming a polydispersed core and monodispersed shell. The second form factor is the same, with Fe$_3$O$_4$-core/OA-shell structure. During the fitting, we fix the scattering length densities of the Au, Fe$_3$O$_4$, OA, and d-toluene to their bulk values in order to reduce the number of free parameters. The best fit is represented by the solid line in Fig. 4(a). SANS measurements indicate the presence of spherical Au nanoparticles with $R = 2 \pm 1$ nm and small clusters of Fe$_3$O$_4$ with $R = 1 \pm 0.3$ nm. The size of the Au nanoparticles is in excellent agreement with the TEM results. The dashed line in Fig. 4(a) is the fit with the form factor of Au nanoparticles only, which poorly reproduces the data at low q. The implication is that both form factors for spherical nanoparticles of Au and Fe$_3$O$_4$ are required to obtain the best fit to our data. Figure 4(b) shows SANS intensity of the Au-3 sample, after nucleation of Fe$_3$O$_4$ nanoparticles has been completed. Again, we used a sum of two models to describe the scattering pattern from the dumbbell nanoparticles. Each model is a form factor for core-shell nanoparticles [49] multiplied by the structure factor described by Teixeira [50] for the fractal-like aggregates. The form and structure factor are calculated for Au and Fe$_3$O$_4$ nanoparticles and SANS intensity is then fitted to the sum of both models. Inclusion of the structure factor added two more free parameters, fractal dimension D and correlation length L. In order to reduce the number of free parameters and obtain a stable fit, we fixed the size of Au nanoparticles and ligand-shell thickness to the values obtained from the refinements of SANS data for the as-synthesized Au-3 sample (Table II). The scattering length densities of Au, Fe$_3$O$_4$, OA, and d-toluene were also fixed. The best fit is depicted as a solid line in Fig. 4(b). The radius of Fe$_3$O$_4$ nanoparticles derived from the fit is $R = 8.5 \pm 1.5$ nm. We note that our model fails to reproduce the experimental data at $q > 0.7$ Å^{-1} because it ignores an average of the dumbbells over all possible orientations [51,52]. Moreover, the polydispersity of nanoparticles

derived from refinements are likely overestimated because smearing effects of the finite-q resolution were not taken into account. Development of a more realistic two-phase model with polydisperse core-shell building blocks is currently underway. The quality of the SANS fit is ambiguous at higher q, and thus we repeated the small-angle measurements using synchrotron x rays [Fig. 4(c)] for both dumbbell samples. The dumbbell nanoparticles provide the core contrast for x rays [see inset Fig. 4(c)]; therefore we used a simplified two-fractals model for polydisperse core particles without a shell [50]. The SAXS measurement of the sample Au-3 finds that the size of Au ($R = 2.7 \pm 0.7$ nm) nanoparticles is consistent with the SANS and TEM results. The size of Fe$_3$O$_4$ nanoparticles is found to be 9.8 ± 1.2 and 9.3 ± 1.2 nm for the samples Au-3 and Au-4, respectively (Table III). The values are somewhat higher than the values obtained by TEM measurements. Magnetite has a brighter contrast in TEM and the presence of the overlapping particles makes it difficult

TABLE II. Results of the SANS refinements of the as-synthesized Au-3 sample and the same sample after 12 hours, where R_{core} is the radius of the core, σ is the core polydispersity, t_{shell} is the thickness of the shell, D is the fractal dimension, L is the correlation length, and SLD_{core}, SLD_{shell}, and SLD_{solv} are the neutron-scattering length densities for the core, shell, and solvent, respectively.

| | Au-3 (fresh) | | Au-3 | |
Sample	Au	Fe$_3$O$_4$	Au	Fe$_3$O$_4$
Scale factor	0.02(2)	1.27(1)	0.016(8)	0.115(3)
R_{core} (nm)	2.73(2)	0.61(3)	2.73	8.49(63)
σ	0.46(2)	0.49(2)	0.12(1)	0.17(1)
t_{shell} (nm)	0.29(3)	0.27(2)	0.29	6.13(73)
D			1.0(4)	6.0(5)
L (nm)			0.94(5)	0.47(6)
SLD_{core} (Å^{-2})	4.56×10^{-6}	6.84×10^{-6}	4.56×10^{-6}	6.89×10^{-8}
SLD_{shell} (Å^{-2})	8.87×10^{-8}	8.87×10^{-8}	8.87×10^{-8}	8.87×10^{-8}
SLD_{solv} (Å^{-2})	5.66×10^{-6}	5.66×10^{-6}	5.66×10^{-6}	5.66×10^{-6}
bkg (cm^{-1})	0	0.45	0	0.18

TABLE III. Summary of the SAXS refinements for Au-3 and Au-4 samples, at room temperature in ambient conditions. R is the block radius in nanometers (nm), σ is the block polydispersity, D is the fractal dimension, L is the correlation length, and SLD and SLD_{solv} are the scattering length density of the block and solvent, in inverse Angstroms (Å^{-1}), respectively. The units are nanometers (nm) and Angstroms (Å).

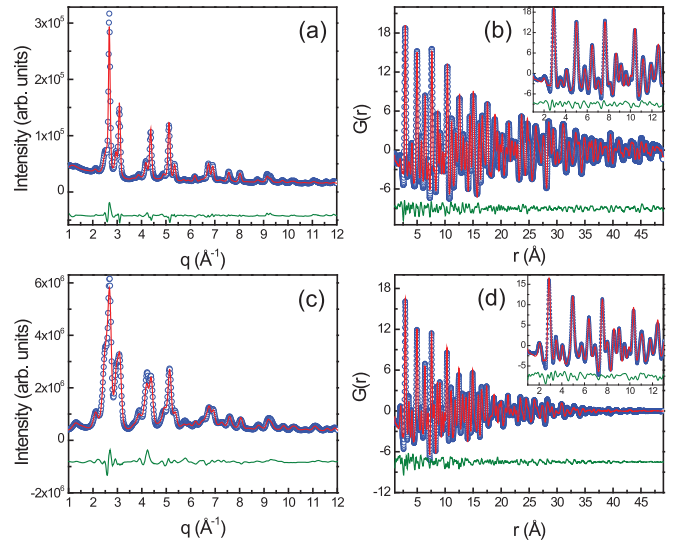| Phase	Au-3		Au-4	
	Au	Fe_3O_4	Au	Fe_3O_4
Scale	0.005(1)	0.27(1)	0.003(1)	0.23(1)
R (nm)	2.78(1)	9.87(1)	3.80(2)	9.30(4)
σ	0.25(2)	0.12(1)	0.11(1)	0.12(2)
D	1.6(2)	1.22(1)	3.3(2)	2.2(1)
L (nm)	62.1(2)	233(3)	62.0(3)	288(11)
SLD (Å^{-2})	1.32e-4	4.11(11)e-5	1.32e-4	4.11(9)e-5
SLD_{solv} (Å^{-2})	7.96e-6	7.96e-6	7.96e-6	7.96e-6

FIG. 5. (Color online) The Rietveld and PDF analysis for (a),(b) sample Au-4 and (c),(d) sample Au-3, with experimental data in open circles, calculated pattern in red, and difference curve in green. Insets in (b) and (d) are the same data for $r = 1-13$ Å.

to reliably extract dimensions of Fe_3O_4 nanoparticles on a limited sample area.

If magnetic interactions between nanoparticles are significant, the scattering intensity would depend on the magnitude of an applied magnetic field [53–56]. We subject the solution of the dumbbell nanoparticles into the magnetic field and find no considerable difference between SAXS intensities measured at 0 and 1.2 T for both samples. Therefore, the interparticle interactions play no role in the magnetic processes, including enhancement of T_B in the dumbbell nanoparticles. SANS results indicate that Au nanoparticles are coated with the surfactant in the dumbbell nanoparticles. It is unlikely, however, that the ferromagnetism was induced in Au nanoparticles by the ligands. The ZFC $M(H)$ measurements of the mixture of Au and Fe_3O_4 nanoparticles showed the ferrimagneticlike response, with the coercivity field and saturation magnetization both consistent with the values reported for the bulk Fe_3O_4 [21]. We tried to improve the SANS and SAXS fits by introducing the FeO phase, which is evident from magnetization measurements, by adjusting the scattering cross section of the Fe_3O_4 nanoparticles. For x rays, the difference between the FeO and Fe_3O_4 phases in electron density is about 10% (1637 and 1478 e/nm^3, respectively). The contrast is even weaker for neutrons, with the difference in SLD less than 6% (7.3×10^{-6} and 6.9×10^{-6} cm^{-2}). The quality of the SANS and SAXS fits showed no improvements when the FeO phase was added. Thus, we carried out synchrotron x-ray diffraction experiments on the dumbbell nanoparticles. Fe_3O_4 has an inverse spinel structure, while FeO adopts the cubic structure of NaCl. Both phases should be easily distinguishable with synchrotron x-ray diffraction. Rietveld refinements of the diffraction data for both samples are shown in Figs. 5(a) and 5(c). The best fit was obtained using three cubic phases: Au (space group Fm-$3m$, Inorganic Crystal Structure Database (ICSD) collection code 52249), magnetite Fe_3O_4 (Fd-$3m$, ICSD code 27898), and wüstite FeO (Fm-$3m$, ICSD code 27237). The scale factor, lattice constants, and anisotropic displacement parameters (ADPs) were refined for each phase. The constant wavelength x-ray GSAS profile function type 3 was used to describe the peak shapes [57]. The results of the refinements are summarized in

Table IV. The lattice constant of the Au phase in the Au-4 sample is close to the reported bulk value of 4.084 Å, while in the sample Au-3 with smaller Au nanoparticles, it is significantly lower (4.051 Å). Conversely, the lattice constant of Fe_3O_4 nanoparticles in the Au-3 sample is in excellent agreement with the bulk value of 8.396 Å, while it is larger for sample Au-4 (8.477 Å). The ADP of oxygen in magnetite is a factor of 20 larger compared to the ADP of Fe in the a and b sites, and has a substantial uncertainty. This is because light elements such as oxygen provide little contrast for x rays, making reliable refinement of ADP difficult. We attempted to refine the crystallite size broadening parameter to estimate the particle size for each phase. We found this parameter to be highly correlated with the Gaussian terms in the profile function, resulting in unphysically large dimensions of Au nanoparticles. The estimated crystallite size of FeO was 5.3 and 3.6 nm for Au-4 and Au-3 samples, respectively. Larger crystallite size of antiferromagnetic FeO can explain higher H_{EB} in the Au-4 sample; however, we stress that the peak broadening is not directly related to a physical size of nanoparticles. Any relation to a physical size relies on correcting the extracted value with an assumption with regard to the crystallite shape, which is unknown for FeO. Besides, the peak broadening induced by finite crystallite size is rarely Gaussian only [58,59].

Our Rietveld refinements clearly indicate the presence of the FeO phase, which is not chemically stable and can be spontaneously oxidized into ferrimagnetic Fe_3O_4, antiferromagnetic α-Fe_2O_3 (hematite), or ferrimagnetic γ-Fe_2O_3 (maghemite) phases [60]. All three phases have distinctive magnetic properties and might contribute to the exchange biasing in the dumbbell nanoparticles. It is challenging to distinguish between the maghemite and magnetite phases using a standard Rietveld refinement of a powder x-ray diffraction data due to their similar crystallinity; however, these issues can be overcome by using high-energy synchrotron x rays [36,61]. The scattering structure factor $S(q)$, with the

TABLE IV. Summary of the Rietveld refinements depicted in Fig. 5. Goodness of the fits are $R_{wp} = 0.046$, $R_p = 0.035$, $\chi^2 = 55.62$ for the sample Au-4, and $R_{wp} = 0.054$, $R_p = 0.044$, $\chi^2 = 1913$ for the sample Au-3. The units are Angstroms (Å).

	Au-4			Au-3		
Sample	Au	Fe₃O₄	FeO	Au	Fe₃O₄	FeO
Scale	0.982	0.359	5.149	0.116	0.531	1.360
a,b,c (Å)	4.0847(3)	8.4774(68)	4.2824(16)	4.0504(5)	8.3913(51)	4.2327(15)
U_{iso} (Au) (Å^2)	0.0295(3)			0.0126(5)		
U_{iso} (O) (Å^2)		0.8000(370)	0.0148(49)		0.7948(315)	0.0031(24)
U_{iso} (Fe$_a$) (Å^2)		0.0254(33)	0.0502(32)		0.0331(32)	0.0021(10)
U_{iso} (Fe$_b$) (Å^2)		0.0474(38)			0.0500(72)	

corrections for background scattering, x-ray transmission, and Compton scattering, was obtained from the same diffraction data using the PDFgetX2 software package [62]. The PDF was calculated by a Fourier transformation of $S(q)$ with $q_{max} = 25$ Å^{-1}:

$$G(r) = \frac{2}{\pi} \int_{q_{min}}^{q_{max}} q[S(q) - 1] \sin(qr)dq. \qquad (1)$$

The PDF for both samples is plotted in Figs. 5(b) and 5(d). We used the averaged structures obtained from the Rietveld refinements as a starting point in the PDF data analysis. The scale factor, lattice constant, ADPs, and linear atomic correlation factor δ_1 were refined for each phase in the range of 1–50 Å. The model with three cubic phases of Au, FeO, and Fe₃O₄ provides a good description of the data with the discrepancy of $R_w = 0.14$ and $R_w = 0.11$ for samples Au-3 and Au-4, respectively (Table V). The convergence of the $G(r)$ function at higher r due to the finite size of our particles and limited q resolution [33,63] prevented us from refining dimensions of Fe₃O₄ nanoparticles, which were fixed to the values obtained with SANS/SAXS experiments.
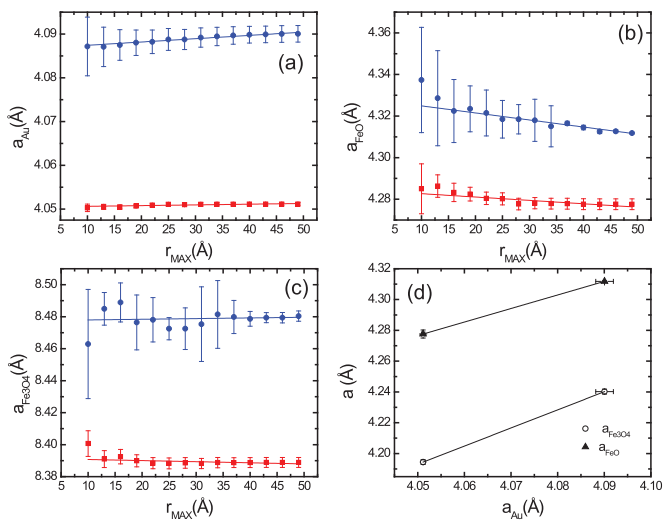

FIG. 6. (Color online) Lattice constants of (a) Au, (b) FeO, and (c) Fe₃O₄ nanoparticles obtained from PDF refinement as a function of r_{max} for Au-4 (●) and Au-3 (■) samples. (d) The lattice constant of Fe₃O₄ (○) and FeO (▲) as a function of the Au lattice constant for both samples. Solid lines are linear fits to the data.

The lattice parameters derived from PDF refinement are in good agreement with those reported from Rietveld analysis. The results indicate a substantial difference between lattice constants of all three phases for the Au-3 and Au-4 samples. The lattice constant of Au (4.09 Å) in Au-4 is close to the value of bulk Au (4.08 Å), while it is smaller (4.05 Å) in sample Au-3 [Fig. 6(a)]. We conclude that the reduction in size of the Au nanoparticle leads to a reduction of its lattice constant, consistent with the previous reports [64]. It is not the case for Fe₃O₄ nanoparticles. Although they are of similar size in both samples, the lattice constant of magnetite in the sample Au-4 is larger than in the sample Au-3 [Fig. 6(b)]. The same tendency persists for the FeO phase [Fig. 6(c)]. Overall, there is a clear correlation of the iron-oxide lattice constants with the lattice constant of the Au seed nanoparticles [Fig. 6(d)].

Our PDF model assumes a mixture of three spheres with no interface or epitaxial linkage between them. It means that possible bonds at the Au/FeO and Fe₃O₄/FeO interfaces are not included in the model. It explains the nonrandom difference curve, particularly at low r [see insets in Figs. 5(b) and 5(d)] and suggests that not every interatomic distance is taken into account by our model. However, the model is good enough to clearly discriminate various phases of iron oxide and provide reliable crystallographic information about dumbbell nanoparticles on a local scale.

IV. DISCUSSION

Previous magnetization measurements of Au-Fe₃O₄ dumbbell and flowerlike nanoparticles suggested the altered magnetic state of Fe₃O₄ nanoparticles as an origin of the exchange bias effect [9,10,24,26]. The ferrimagnetic state of bulk Fe₃O₄ is a result of two competing interactions: (i) AFM interactions via superexchange between Fe ions in the tetrahedral (A) and octahedral (B) sites, and (ii) FM interactions via double exchange between Fe ions in the octahedral sites. The exchange integrals for the bulk magnetite are $J_{AB} = -22$ K and $J_{BB} = 3$ K [21]. They depend on $\cos^2\phi$, where ϕ is the cation-anion-cation angle, as well as on the cation-anion distance. The quantitative dependence of integrals on angle and distance is unclear, but in general smaller cation-anion distances and angles close to 180° lead to the largest values of J. The magnetic state of Fe₃O₄ nanoparticles is very different compared to its bulk counterpart. Finite-size effects result in a

TABLE V. Summary of the x-ray PDF refinement results for Au-3 and Au-4 samples for $r = 1 - 50$ Å. The instrument resolution Qdamp and Qbroad, as well as $q_{max} = 23$ Å^{-1} were fixed during the refinements.

Phase	Au-3			Au-4		
	Au	Fe_3O_4	FeO	Au	Fe_3O_4	FeO
Scale factor	1.11(2)	0.39(2)	0.21(2)	1.42(14)	0.22(15)	0.12(8)
a,b,c (Å)	4.052(1)	8.389(3)	4.278(3)	4.090(2)	8.481(3)	4.312(1)
δ_1	1.54(7)	1.81(12)	1.82(14)	1.72(21)	1.08(21)	2.94(75)
R (nm)	3.6(2)	8.4	0	5.4 (1.4)	8.4	0
$U_{11,22,33}$ (Au) (Å^2)	0.009(2)			0.0117(14)		
$U_{11,22,33}$ (O) (Å^2)		0.0143(23)	0.048(7)		0.0163(63)	0.0354(75)
$U_{11,22,33}$ (Fe$_a$) (Å^2)		0.0084(13)	0.017(2)		0.0106(27)	0.0212(23)
$U_{11,22,33}$ (Fe$_b$) (Å^2)		0.0165(18)			0.0352(65)	
R_w	0.14			0.11		

smaller coordination number of surface atoms, which weakens exchange interactions. Missing cations or anions imbalance the number of antiferromagnetic and ferromagnetic sublattices, leading to a distorted arrangement of the surface spins. The variation of the ϕ angle due to internal tensile strain can further affect the strength of the exchange interactions [65]. The combination of these effects leads to the magnetic state of Fe_3O_4 nanoparticles best described by the ferrimagnetically ordered core and canted-spin shell [15].

In principle, coupling between ordered core and disordered shell can lead to the exchange bias effect [66]. However, previous reports found no evidence of the exchange bias in the single-component Fe_3O_4 nanoparticles with size larger than 6 nm, in agreement with our results [14,19,66]. This lack of exchange coupling between core and shell is likely due to a small number of surface spins. The exchange bias effect was predicted for 1.25 nm Fe_3O_4 nanoparticles, in which 55% of all atoms reside at the surface [67,68]. For 9.8 nm Fe_3O_4 nanoparticles used in our work, this number is dramatically decreased down to 10%. However, in the dumbbell nanoparticles, the number of the canted spins can be increased at the interface with Au nanoparticles. Canted spins, which are characterized by possibly shorter cation-anion distances and variation of ϕ angle, can be probed by analysis of the PDF data. In the PDF model with Au and Fe_3O_4 phases only, we refined positions of Fe and O atoms in the dumbbell nanoparticles. The refinement was done for the range

FIG. 7. (a) The STEM image of a Fe_3O_4 nanoparticle in the sample Au-3. (b) The same image at higher magnification.

$r = 1.5 - 50$ Å, with the step of 3 Å. Such strategy allows us to refine the smaller volumes of Fe_3O_4 nanoparticles at the time, rendering the fact that only a small portion of interface atoms can be distorted. Refinements of the position of Fe atoms in both tetrahedral and octahedral sites show no apparent r dependence and remain a constant within experimental error. We found the angle between *A-B* Fe ions, $\phi_{AB} = 124.5(3)°$, in excellent agreement with the value of $125°$ reported for the bulk magnetite [21,69]. The refined Fe-O and Fe-Fe distances of the Au-3 sample were 2.08(1) and 2.98(1) Å. Both of them are in excellent agreement with the values determined from PDF refinements of bulk Fe_3O_4: 2.07 and 2.97 Å [69]. Of course, it is worth noting that refinements of the PDF data with only two phases of Au and Fe_3O_4 resulted in rather poor quality of fits, with $R_w = 0.35$ and 0.42 for the samples Au-3 and Au-4, respectively. Only the introduction of the third FeO phase improved the fits and reduced R_w down to 0.14 and 0.11. Nevertheless, we tried to refine the Fe and O positions in the three-phase model, but only a marginal improvement of the fit was observed. It is fair to say that the crystal structure of Fe_3O_4 nanoparticles in the dumbbell samples remains similar to its bulk counterpart, at least within the accuracy of our model.

The antiphase boundaries (APBs) were responsible for the EB effect observed in thin films of Fe_3O_4 deposited on MgO substrate [70]. The lattice constants of Fe_3O_4 are almost double those for MgO and Au. Thus, heteroepitaxy is possible in both cases and the formation of APBs can be expected in Fe_3O_4 nanoparticles in the dumbbell samples. The APBs are stacking faults naturally occurring during the island growth mode in heteroepitaxy. Because of the difference in lattice constant and symmetry, the different Fe_3O_4 islands can be shifted or rotated during the growth [70]. Across APBs, the AFM interactions (J_{AA}) between *A* sublattice Fe ions are greatly increased [21]. Consequently, they can be exchange coupled to the neighboring ferromagnetic regions, where FM interactions (J_{BB}) are dominant. The APBs can be directly observed with high-resolution transmission electron microscopy (HRTEM) or a scanning transmission electron microscope (STEM) as the regions of irregular shape with a darker contrast (see, for example, HRTEM images of Fe_3O_4 thin films in [71]). Figure 7 shows the STEM images of a single Fe_3O_4 nanoparticle in the Au-3 sample. Lines of atoms extend in perfect registry
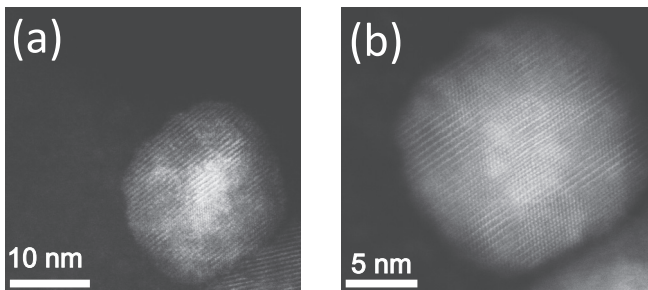
from the core to the surface and no signs of APBs are evident [Fig. 7(b)]. The stacking faults associated with APBs can be modeled in the analysis of the PDF data. For example, in CdSe nanoparticles, density faults as large as 50% were observed as unphysically large values of anisotropic atomic displacement parameters U_{33} for Se atoms in the PDF model [72]. We found no improvements of the fit with introducing anisotropic atomic displacement parameters ($U_{11} = U_{22} \neq U_{33}$) for both O and Fe atoms. However, U_{ii} values obtained for Fe atoms in the dumbbell nanoparticles are twice as large (see Table V) compared to the values obtained for the bulk. Based on STEM studies and analysis of the PDF data, we must conclude that the APBs are absent in our dumbbell nanoparticles and cannot account for the EB effect. Overall, we can reject the altered magnetic state of Fe$_3$O$_4$ nanoparticles as the origin of the exchange bias effect in the dumbbell nanoparticles.

Magnetite can be oxidized into hematite (α-Fe$_2$O$_3$). Hematite crystallizes in the rhombohedral structure and becomes AFM below 260 K [73]. In principle, the coexistence of the AFM hematite and FiM magnetite phases in the dumbbell nanoparticles can explain the EB effect. However, the rhombohedral structure of hematite can be unambiguously distinguished from the cubic structure of magnetite with x-ray diffraction experiments. Moreover, our reference bulk sample consisted of 80% of Fe$_3$O$_4$ and 20% of α-Fe$_2$O$_3$, which was measured in the identical experiential conditions as the dumbbell nanoparticles. Two phases were clearly detectable and provided an excellent reference. Rietveld and PDF refinements found no evidence of the hematite phase in the dumbbell nanoparticles. It is not surprising, considering that our dumbbell nanoparticles have not been exposed to the temperatures as high as 550°C, which are required for oxidation of Fe$_3$O$_4$ into α-Fe$_2$O$_3$ [74]. We also tried to introduce the maghemite phase (γ-Fe$_2$O$_3$) into the PDF refinements. Maghemite has a very similar crystal structure to magnetite and the coexistence of the two phases has been previously reported in iron-oxide nanoparticles [75]. However, the best quality of the fit obtained with dual γ-Fe$_2$O$_3$/Fe$_3$O$_4$ phases was $R_w = 0.32$, while the model with FeO/Fe$_3$O$_4$ phases resulted in a much better fit with $R_w = 0.14$ (for the sample Au-3).

The x-ray diffraction and magnetization measurements suggest the presence of an antiferromagnetic FeO phase in the dumbbell nanoparticles. Hence, we conclude that the exchange bias effect observed in the dumbbell nanoparticles is the result of the coupling between antiferromagnetic FeO and ferrimagnetic Fe$_3$O$_4$ phases, consistent with the previous reports on FeO/Fe$_3$O$_4$ composite nanostructures [34,36,61,76–80]. The question is what is the origin of the FeO phase in our dumbbell nanoparticles? The nanostructures with FeO and Fe$_3$O$_4$ phases can be obtained either by oxidation of FeO nanoparticles or by reduction of Fe$_3$O$_4$ nanoparticles. Sun *et al.* oxidized the surface of FeO nanoparticles by introducing dry air into the solution of FeO nanoparticles at 25, 60, and 100 °C to synthesize FeO-core/Fe$_3$O$_4$-shell nanoparticles [34]. Similarly, the FeO nanoparticle solution was washed out several times and exposed to air for 5–120 days, resulting in the formation of the FeO-core/Fe$_3$O$_4$-shell structures [36,61,77,79]. The synthesis of FeO/Fe$_3$O$_4$ nanoparticles consists of two steps: the synthesis of FeO nanoparticles and their further oxidation in air. The synthesis of FeO is achieved

by decomposing Fe(CO)$_5$ in a solvent mixture that had a weak oxidizing agent "pyridine N-oxide" that partially oxidizes the Fe to FeO [77]. In our samples, the Fe(CO)$_5$ was decomposed under an Ar atmosphere and the oxidizing agent was absent. Thus, the formation of FeO nanoparticles in the dumbbell nanoparticles prior to oxidation is unlikely. Finally, we used the same synthesis to obtain free Fe$_3$O$_4$ nanoparticles, where no evidence of the FeO phase was found. If single-component Fe$_3$O$_4$ nanoparticles were formed after oxidation was completed, another plausible explanation for the coexistence of FeO and Fe$_3$O$_4$ phases is a partial reduction of magnetite. The Fe$_3$O$_4$-core/FeO-shell nanoparticles were synthesized at 550 °C in the ultrahigh vacuum by partially reducing the surface of Fe$_3$O$_4$ nanoparticles into FeO [81]. Obviously, this scenario can be excluded in our samples because they have not been exposed to such high temperature and vacuum. In what follows, we suggest that the partial reduction of Fe$_3$O$_4$ into FeO occurs at the interface with Au nanoparticles.

Because of the catalytic applications of Au nanoparticles, their electronic structure has been intensively studied [18,26,27,82]. The charge transfer from Au nanoparticles to the adjacent metal in bimetallic nanostructures or to the capping agent dramatically modifies the electron configuration of Au on the nanoscale. The famous example is the ferromagnetism observed in small Au nanoparticles coated with the thiol-group surfactant. The strong charge transfer from Au surface atoms to S resulted in the generation of holes in $5d$ orbitals. Those holes were able to sustain ferromagnetic moments even at room temperature [18]. Similarly, the ferromagnetic behavior was observed in Au$_{48}$Pt$_{52}$ nanowires, due to d-charge transfer from the Au to the Pt site [83]. The Au nanoparticles were also found to change the electronic properties of the oxide substrates. For instance, Au nanoparticles deposited on a TiO$_2$ substrate showed very high catalytic activity because Au nanoparticles partially reduce TiO$_2$ at the interface. This interface is believed to be the most active part of the catalyst [82]. The charge transfer from Au to Fe$_3$O$_4$ was observed in Au-Fe$_3$O$_4$ nanostructures, including dumbbells, with x-ray absorption techniques [26,27]. The charge transfer resulted in an increase of the Fe^{2+} valence state in magnetite and the formation of Au-O and Au-Fe bonds, presumably across the Au/Fe$_3$O$_4$ interface [26]. In the magnetite, for every four O^{2-} anions, there are two Fe^{3+} and one Fe^{2+} cations. If the charge balance is violated by the increased number of Fe^{2+} cations, the reduction of magnetite can occur to lower electrostatic energy: Fe$_3$O$_4$ → 3FeO + O. As a result, the FeO phase and excess of oxygen are formed. The reduction of magnetite nanoparticles takes place at the Au/Fe$_3$O$_4$ interface. The limited diffusion path of $5d$ electrons transferred from Au and confines the formation of the FeO phase to the vicinity of the interface region; thus the Fe$_3$O$_4$/FeO structure is sustained. STEM measurements of Au-3 sample provide limited support for this conclusion, showing the contrast variation across a single magnetite nanoparticle [Fig. 7(a)]. The interior of this nanoparticle appears to be brighter than the exterior, suggesting a Fe$_3$O$_4$-rich-core and a FeO-shell structure [79].

The reduction of Fe$_3$O$_4$ at the interface with Au nanoparticles will lead to the excess of oxygen atoms. We suggest that those oxygen atoms formed Au-O bonds at the interface between gold and magnetite. The formation of Au-O bonds
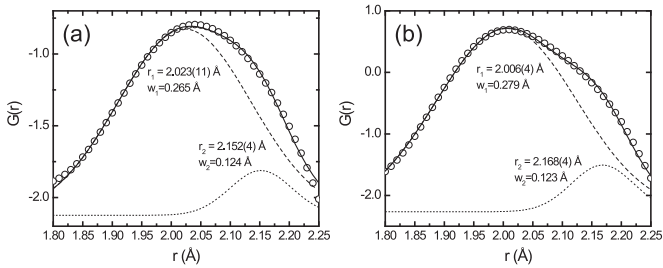
FIG. 8. Fits of the low-*r* region of x-ray PDF for samples (a) Au-4 and (b) Au-3. The dashed line is the broad Gaussian and the dotted line is the narrow Gaussian. The solid line is the sum of both.

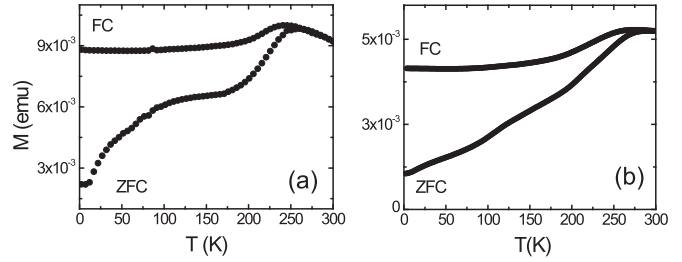

FIG. 9. Comparison of ZFC and FC *M*(*T*) magnetizations for (a) a fresh Au-3 sample and (b) the same sample aged for 23 months.

in the dumbbell nanoparticles was previously observed with x-ray photoemission spectroscopy (XPS) measurements [26]. The formation of the Au-O bonds can also explain the imperfection of our PDF model. The model used for refinement of the x-ray PDF could not reproduce the first peak at $r \sim 2.01$ Å for both samples [see insets in Figs. 5(b) and 5(d)]. The position of this peak does not correspond to the C-C bond length of 1.540 Å, which was reported for the oleic-acid-coated Fe_3O_4 nanoparticles [75]. The best fit of the peak consists of two separate Gaussian peaks with very different widths: broad G_1, which is responsible for the majority of the intensity in this *r* range, and G_2, which is less intense with the peak position shifted towards larger distances (Fig. 8). The position of the G_2 peak in the sample Au-4 corresponds to the nearest-neighbor Fe-Fe distance of ~2.15 Å in the magnetite. The width of this peak is consistent with the ADP parameter for this phase at 300 K. The position of the G_1 peak, however, cannot be indexed with any interatomic distances in all three phases present in our model. The width of the G_1 is a factor of two larger than that of G_2 for both samples. If the G_1 peak were to belong to a crystallographic model, one would expect it to be narrower compared to the G_2 peak due to highly correlated interatomic motions which sharpen the peaks at lower *r*. It is certainly not the case. The position of the G_1 peak is equal to 2.023(11) and 2.006(4) Å for the Au-4 and Au-3 samples, respectively. Both are comparable with the 2.03(7) Å value reported for the Au-O bonds in Fe_3O_4-Au nanostructures [26]. Although the location of Au-O bonds cannot be determined from PDF measurements, we hypothesize that they are formed at the Au/Fe_3O_4 interface as a result of the partial reduction of the magnetite phase. Figure 6(a) shows that the lattice constant of Au nanoparticles is considerably reduced in smaller nanoparticles (sample Au-3) compared to the larger ones (Au-4). It is in agreement with previous reports, which suggested that the lattice size of a metal nanoparticle shrinks with decrease of a particle size [84]. In contrary, the lattice size of small metal-oxide nanoparticles expands, presumably due to modifications of the attractive potential [85–87]. The lattice constant of Fe_3O_4 nanoparticles is very different in the samples Au-3 and Au-4, even though they are of the same size in each sample. The lattice constant $a = 8.481$ Å of Fe_3O_4 nanoparticles in the sample Au-4 is larger than the value of 8.395 Å in the bulk magnetite. In the sample Au-3, the lattice constant $a = 8.389$ Å is *smaller* than the bulk value. Apparently, finite-size effects have no obvious impact on the lattice dimensions of Fe_3O_4 nanoparticles

in the dumbbell samples. We think that such a significant difference in lattice size of Fe_3O_4 nanoparticles is due to their epitaxial linkage to the seed Au nanoparticles. In thin films, the deposited layer adopts the crystalline structure of a substrate during epitaxy. The same effect was observed in the FeO nanoparticles deposited on Au and Pt substrates. The lattice of FeO nanoparticles was found to be larger when deposited on the Au(111) substrate than on the Pt(111) substrate because the lattice constant of Au is larger than the one of Pt. Our findings suggest that this is the case for the dumbbell nanoparticles as well. The lattice constants of both FeO and Fe_3O_4 are correlated with the lattice constant of the seed gold nanoparticles; however, more data points are needed to quantify this correlation [Fig. 6(d)].

The reduction of Fe_3O_4 to FeO presumably occurs across the Au/Fe_3O_4 interface, which is larger in sample Au-4; thus it may explain the enhancement of H_{EB} observed in this sample. More spins at the interface are exchange coupled and higher magnetic fields are required to reverse the magnetization of the FiM layer [78]. The bulk wüstite FeO is unstable and can spontaneously undergo phase transformation into the spinel-like structure of maghemite or magnetite after 10 days. [79]. Therefore, the effect of the interfacial area on H_{EB} can be directly probed by magnetization measurements of the aged dumbbell sample. Figure 9 compares *M*(*T*) measurements of the freshly synthesized Au-3 sample and the same sample aged for 23 months. There is no clear peak in the ZFC magnetization at $T_N = 190$ K of the FeO phase for the aged sample. The FC magnetization loop shows the negative shift in the horizontal direction, with smaller $H_{EB} = 980$ Oe compared with $H_{EB} = 1350$ Oe of the as-synthesized Au-3 sample (Fig. 3). We hypothesize that the reduction of H_{EB} is related to FeO volume change. For example, decreasing the FeO volume resulted in a reduction of H_{EB} in thin-film systems [78]. Interestingly, the FeO phase can still be detected in nanoparticles even after 23 months, indicating that in contrast to the bulk FeO, only part of FeO transforms into Fe_3O_4, consistent with the previous reports [23,88]. The partial reduction presumably occurs due to the diffusion of Fe^{2+} and Fe^{3+} ions in the oxygen sublattice and charge transfer between Fe ions of different valence [77].

The exchange bias effect in composite nanoparticles is far more complex than in thin films, even of the same composition [89]. For example, Co-core/CoO-shell nanoparticles show nonmonotonic dependence of H_{EB} on the size of the Co core, in contrast to thin films where $H_{EB} \sim 1/t_{FM}$, where t_{FM} is the thickness of the FM layer [78]. The nonmonotonic depen-
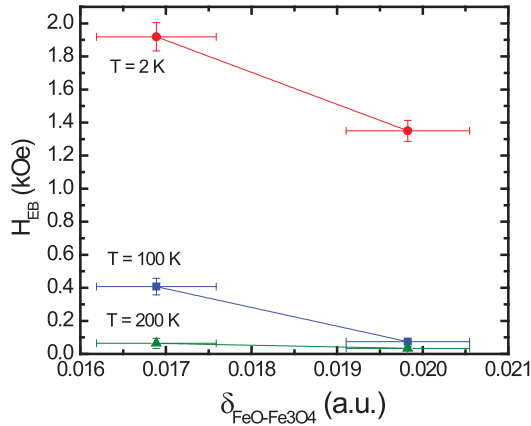
FIG. 10. (Color online) The exchange bias field H_{EB} as a function of lattice mismatch δ between FeO and Fe$_3$O$_4$ at 2 K (●), 100 K (■), and 200 K (▼).

dence can be understood by appealing to neutron-diffraction measurements carried out on Co/CoO nanoparticles, which demonstrated a relation between H_{EB} and strain induced by the lattice mismatch between the Co and CoO shell [90]. Strikingly, Fig. 10 shows the dependence of H_{EB} on the lattice mismatch between FeO and Fe$_3$O$_4$ for both dumbbell samples at various temperatures, where larger H_{EB} are observed in the sample Au-4 with a smaller lattice mismatch. We hypothesize that this lattice mismatch can be responsible for the strain-induced magnetic moment at the Fe$_3$O$_4$/FeO interface, not unlike in Co/CoO nanoparticles [12]. Presumably, the interface magnetic moment is lower in sample Au-4 with the bulklike Au seed nanoparticles. It is, however, increased in the sample Au-3, where the smaller lattice constant of Au nanoparticles leads to a more canted interface between FeO and Fe$_3$O$_4$. The magnitude and relation of this interface magnetic moment with the volume of the FeO phase are yet to be studied with neutron-diffraction experiments. If this relation is demonstrated, it opens new ways to control H_{EB} in the dumbbell nanoparticles by simply changing the dimensions of Au seed nanoparticles, which is a simpler way to achieve higher H_{EB} compared to synthesizing flowerlike structures with poorly controlled magnetic state [11].

V. CONCLUSIONS

By using a combination of magnetization, SANS, SAXS, x-ray PDF, and STEM measurements, we elucidated the origin of the EB effect in the Au-Fe$_3$O$_4$ dumbbell nanoparticles, with similar size of Fe$_3$O$_4$ nanoparticles (9.8 nm) and different sizes of the seed Au nanoparticles, 4.1 and 2.7 nm, for samples Au-4 and Au-3, respectively. Both dumbbell samples show similar $T_B = 285$ K and a clear AFM-type transition at 190 K, corresponding to the Néel temperature of FeO. The Rietveld and PDF analysis of the synchrotron x-ray diffraction data confirmed the presence of the FeO phase in both dumbbell nanoparticles, which is unstable and diminishing over time. The origin of the FeO phase is due to the charge transfer from Au to Fe$_3$O$_4$, which increases the number of Fe^{+2} ions in magnetite. This leads to the formation of FeO via reduction of the Fe$_3$O$_4$ phase. The excess of the oxygen during the reduction

forms Au-O bonds, as evident from the analysis of PDF data at lower r. The independent confirmation of the Fe$_3$O$_4$/FeO interface was obtained with STEM, which showed the Fe$_3$O$_4$-rich-core/FeO-shell structure of the magnetite nanoparticles in the sample Au-3. The EB effect was observed for both samples at temperatures below T_B. H_{EB} was found to be the largest in the sample Au-4, with larger size of Au seed nanoparticles. The EB effect was not observed in the reference sample consisting of the mixture of single-component Au and Fe$_3$O$_4$ nanoparticles, and no AFM transition at around 190 K was found. The finite-size effects result in a reduced lattice constant of the Au nanoparticles in the Au-3 sample, while the lattice constant found in the sample Au-4 is similar to the bulk value of Au. The lattice constant of Fe$_3$O$_4$ nanoparticles is reduced in the sample Au-3 as compared with the sample Au-4, despite the same size of Fe$_3$O$_4$ nanoparticles in both samples. The lattice contraction of the FeO phase was observed as well in the sample Au-3. The epitaxial linkage between Fe$_3$O$_4$ and Au nanoparticles leads to the reduction of the lattice constant of Fe$_3$O$_4$, which adopts the smaller lattice volume of Au nanoparticles in the Au-3 sample. The large surface area between the Fe$_3$O$_4$ and FeO phases in the sample Au-4 leads to a higher H_{EB} compared with the sample Au-3. We found evidence that H_{EB} depends on the lattice mismatch between the Fe$_3$O$_4$ and FeO phases; however, more neutron-scattering experiments are needed to understand this dependence. The additional TEM electron energy-loss spectroscopy (EELS) measurements of the dumbbell nanoparticles are being pursued to identify the location and oxidation state of the FeO phase and provide independent conformation for the presence of Au-O bonds. The method has been successfully used in the past to determine oxidation states of transition-metal-oxide systems on a nanoscale [91,92].

[1] K. C.-F. Leung, S. Xuan, X. Zhu, D. Wang, C.-P. Chak, S.-F. Lee, W. K.-W. Ho, and B. C.-T. Chung, Chem. Soc. Rev. **41**, 1911 (2012).

[2] S. M. Janib, A. S. Moses, and J. A. Kackay, Adv. Drug Delivery Rev. **62**, 1052 (2010).

[3] C. Sun, J. S. H. Lee, and M. Zhang, Adv. Drug Delivery Rev. **60**, 1252 (2008).

[4] T. Hasan, P. Rai, S. Mallidi, X. Zheng, R. Rahmanzadeh, Y. Mir, S. Elrington, and A. Khurshid, Adv. Drug Delivery Rev. **62**, 1094 (2010).

[5] C. Xu, B. Wang, and S. Sun, J. Am. Chem. Soc. **131**, 4216 (2009).

[6] C. S. Thaxton, D. G. Georganopoulou, and C. A. Mirkin, Clin. Chim. Acta **363**, 120 (2006).

[7] A. S. K. Hashmi and G. J. Hutchings, Angew. Chem., Int. Ed. Engl. **5**, 7896 (2006).

[8] A. Arcadi, Chem. Rev. **108**, 3266 (2008).

[9] S. Chandra, N. A. F. Huls, M. H. Phan, S. Srinath, M. A. Garcia, Y. Lee, C. Wang, S. Sun, O. Iglesias, and H. Srikanth, Nanotechnology **25**, 055702 (2014).

[10] N. A. Frey, S. Srinath, H. Srikanth, C. Wang, and S. Sun, IEEE Trans. Magn. **43**, 3094 (2007).

[11] N. A. Frey, M. H. Phan, H. Srikanth, S. Srinath, C. Wang, and S. Sun, J. Appl. Phys. **105**, 07B502 (2009).

[12] M. Feygenson, Y. Yiu, A. Kou, K. S. Kim, and M. C. Aronson, Phys. Rev. B **81**, 195445 (2010).

[13] M. Feygenson, A. Kou, L. E. Kreno, A. L. Tiano, J. M. Patete, F. Zhang, M.-S. Kim, V. Solovyov, S. S. Wong, and M. C. Aronson, Phys. Rev. B **81**, 014420 (2010).

[14] G. F. Goya, T. S. Berquo, F. C. Fonseca, and M. P. Morales, J. Appl. Phys. **94**, 3520 (2003).

[15] K. L. Krycka, R. A. Booth, C. R. Hogg, Y. Ijiri, J. A. Borchers, W. C. Chen, S. M. Watson, M. Laver, T. R. Gentile, L. R. Dedon, S. Harris, J. J. Rhyne, and S. A. Majetich, Phys. Rev. Lett. **104**, 207203 (2010).

[16] A. G. Roca, M. P. Morales, K. O'Grady, and C. J. Serna, Nanotechnology **17**, 2783 (2006).

[17] K. Page, Th. Proffen, H. Terrones, M. Terrones, L. Lee, Y. Yang, S. Stemmer, R. Seshadri, and A. K. Cheetham, Chem. Phys. Lett. **393**, 385 (2004).

[18] P. Crespo, R. Litrán, T. C. Rojas, M. Multigner, J. M. de la Fuente, J. C. Sánchez-López, M. A. García, A. Hernando, S. Penadés, and A. Fernández, Phys. Rev. Lett. **93**, 087204 (2004).

[19] R. K. Zheng, G. H. Wen, K. K. Fung, and X. X. Zhang, J. Appl. Phys. **95**, 5244 (2004).

[20] R. H. Kodama, A. E. Berkowitz, E. J. McNiff, and S. Foner, Phys. Rev. Lett. **77**, 394 (1996).

[21] D. T. Margulies, F. T. Parker, M. L. Rudee, F. E. Spada, J. N. Chapman, P. R. Aitchison, and A. E. Berkowitz, Phys. Rev. Lett. **79**, 5162 (1997).

[22] D. T. Margulies, F. T. Parker, F. E. Spada, R. S. Goldman, J. Li, R. Sinclair, and A. E. Berkowitz, Phys. Rev. B **53**, 9175 (1996).

[23] F. Pineider, C. Fernandez, V. Videtta, E. Carlino, A. al Hourani, F. Wilhelm, A. Rogalev, P. D. Cozzoli, P. Ghigna, and C. Sangregorio, ACS Nano **7**, 857 (2013).

[24] E. Umut, F. Pineider, P. Arosio, C. Sangregorio, M. Corti, F. Tabak, A. Lascialfari, and P. Ghigna, J. Magn. Magn. Mater. **324**, 2373 (2012).

[25] J. Nogués, V. Skumryev, J. Sort, S. Stoyanov, and D. Givord, Phys. Rev. Lett. **97**, 157203 (2006).

[26] F. Lin and R. Doong, J. Colloid Interface Sci. **417**, 325 (2014).

[27] M. Kim and H. Song, J. Mater. Chem. C **2**, 4997 (2014).

[28] Y. F. Han, J. H. Wang, D. Kumar, Z. Yan, and D. W. Goodman, J. Catal. **232**, 467 (2005).

[29] S. Peng, Y. Lee, C. Wang, H. Yin, S. Dai, and S. Sun, Nano Res. **1**, 229 (2008).

[30] H. Yu, M. Chen, P. M. Rice, S. X. Wang, R. L. White, and S. Sun, Nano Lett. **5**, 379 (2005).

[31] W. T. Heller, V. S. Urban, G. W. Lynn, K. L. Weiss, H. M. O'Neill, S. V. Pingali, S. Qian, K. C. Littrell, Y. B. Melnichenko, M. V. Buchanan, D. L. Selby, G. D. Wignall, P. D. Butler, and D. A. Myles, J. Appl. Crystallogr. **47**, 1238 (2014).

[32] S. R. Kline, J. Appl. Crystallogr. **39**, 895 (2006).

[33] C. L. Farrow, P. Juhas, J. Liu, D. Bryndin, E. S. Bozin, J. Bloch, Th. Proffen, and S. J. L. Billinge, J. Phys. Condens. Matter **19**, 335219 (2007).

[34] X. Sun, N. F. Huls, A. Sigdel, and S. Sun, Nano Lett. **12**, 246 (2012).

[35] H. Khurshid, S. Chandra, W. Li, M. H. Phan, G. C. Hadjipanayis, P. Mukherjee, and H. Srikanth, J. Appl. Phys. **113**, 17B508 (2013).

[36] S. K. Sharma, J. M. Vargab, K. R. Pirota, S. Kumar, C. G. Lee, and M. Knobel, J. Alloys Compd. **509**, 6414 (2011).

[37] E. P. Wohlfarth, J. Magn. Magn. Mater. **39**, 39 (1983).

[38] M. F. Hansen and S. Morup, J. Magn. Magn. Mater. **184**, 262 (1998).

[39] C. Petit, A. Taleb, and M.-P. Pileni, Adv. Mater. **10**, 259 (1998).

[40] E. Lima, Jr., A. L. Brandl, A. D. Arelaro, and G. F. Goya, J. App. Phys. **99**, 083908 (2006).

[41] P. Tartaj and C. J. Serna, Chem. Mater. **14**, 4396 (2002).

[42] R. P. Borges, W. Guichard, J. G. Lunney, J. M. D. Coey, and F. Ott, J. Appl. Phys. **89**, 3868 (2001).

[43] K. Oguz, P. Jivrajka, M. Venkatesan, G. Feng, and J. M. D. Coey, J. Appl. Phys. **103**, 07B526 (2008).

[44] E. J. W. Verwey, Nature (London) **144**, 327 (1939).

[45] R. Prozorov, T. Prozorov, S. K. Mallapragada, B. Narasimhan, T. J. Williams, and D. A. Bazylinski, Phys. Rev. B **76**, 054406 (2007).

[46] A. Mitra, J. Mohapatra, S. S. Meena, C. V. Tomy, and M. Aslam, J. Phys. Chem. C **118**, 19356 (2014).

[47] P. K. Manna and S. M. Yusuf, Phys. Rep. **535**, 61 (2014).

[48] I. V. Golosovsky, G. Salazar-Alvarez, A. Lopez-Ortega, M. A. Gonzalez, J. Sort, M. Estrader, S. Surinach, M. D. Baro, and J. Nogues, Phys. Rev. Lett. **102**, 247201 (2009).

[49] P. Bartlett and R. H. Ottewill, J. Chem. Phys. **96**, 3306 (1992).

[50] J. Teixeira, J. Appl. Crystallogr. **21**, 781 (1988).

[51] H. Kaya, J. Appl. Crystallogr. **37**, 223 (2004).

[52] H. Kaya and N.-R. deSouza, J. Appl. Crystallogr. **37**, 508 (2004).

[53] A. Guenther, J.-P. Bick, P. Szary, D. Honecker, C. D. Dewhurst, U. Keiderling, A. V. Feoktystov, A. Tschoepe, R. Birringer, and A. Michels, J. Appl. Crystallogr. **47**, 992 (2014).

[54] A. Wiedenmann, J. Appl. Crystallogr. **33**, 428 (2000).

[55] A. Wiedenmann, A. Hoell, M. Kammel, and P. Boesecke, Phys. Rev. E **68**, 031203 (2003).

[56] M. Klokkenburg, B. H. Erne, A. Wiedenmann, A. V. Petukhov, and A. P. Philipse, Phys. Rev. E **75**, 051408 (2007).

[57] L. W. Finger, D. E. Cox, and A. P. Jephcoat, J. Appl. Crystallogr. **27**, 892 (1994).

[58] J. Nanda, S. Sapra, D. D. Sarma, N. Chandrasekharan, and G. Hodes, Chem. Mater. **12**, 1018 (2000).

[59] Z. Kaszkur, Z. Kristallogr. **23**, 147 (2006).

[60] Y. Hou, Z. Xu, and S. Sun, Angew. Chem., Int. Ed. Engl. **46**, 6329 (2007).

[61] D. W. Kavich, J. H. Dickerson, S. V. Mahajan, S. A. Hasan, and J.-H. Park, Phys. Rev. B **78**, 174414 (2008).

[62] X. Qiu, J. W. Thompson, and S. J. L. Billinge, J. Appl. Crystallogr. **37**, 678 (2004).

[63] K. Kodama, S. Iikubo, T. Taguchi, and S. Shamoto, Acta Crystallogr. Sect. A **62**, 444 (2006).

[64] K. Page, Th. Proffen, M. Niederberger, and R. Seshadri, Chem. Mater. **22**, 4386 (2010).

[65] K. Balakrishnan, S. K. Arora, and I. V. Shvets, J. Phys. Condens. Matter **16**, 5387 (2004).

[66] J. Nogués, C. Leighton, and I. K. Schuller, Phys. Rev. B **61**, 1315 (2000).

[67] J. Mazo-Zuluaga, J. Restrepo, F. Muñoz, and J. Mejîa-López, J. Appl. Phys. **105**, 123907 (2009).

[68] J. Mazo-Zuluaga, J. Restrepo, and J. Mejîa-López, J. Phys. Condens. Matter **20**, 195213 (2008).

[69] F. de Boer, J. H. van Santen, and E. J. W. Verwey, J. Chem. Phys. **18**, 1032 (1950).

[70] S. K. Arora, R. G. S. Sofin, A. Nolan, and I. V. Shvets, J. Magn. Magn. Mater. **286**, 463 (2005).

[71] W. Eerenstein, T. T. M. Palstra, T. Hibma, and S. Celotto, Phys. Rev. B **68**, 014428 (2003).

[72] A. S. Masadeh, E. S. Bozin, C. L. Farrow, G. Paglia, P. Juhas, S. J. L. Billinge, A. Karkamkar, and M. G. Kanatzidis, Phys. Rev. B **76**, 115413 (2007).

[73] M. J. Benitez, D. Mishra, P. Szary, G. A. Badini Confalonieri, M. Feyen, A. H. Lu, L. Agudo, G. Eggeler, O. Petracic, and H. Zabel, J. Phys. Condens. Matter **23**, 126003 (2011).

[74] K. J. Gallagher, W. Feitknecht, and U. Mannweiler, Nature (London) **217**, 1118 (1968).

[75] S. Disch, Ph.D. thesis, University of Aachen, 2011.

[76] Z. Swiatkowska-Warkocka, K. Kawaguchi, H. Wang, Y. Katou, and N. Koshizaki, Nano. Res. Lett. **6**, 226 (2011).

[77] F. X. Redl, C. T. Black, G. C. Papaefthymiou, R. L. Sandstrom, M. Yin, H. Zeng, C. B. Murray, and S. P. OBrien, J. Am. Chem. Soc. **126**, 14583 (2004).

[78] J. Nogués and I. Schuller, J. Magn. Magn. Mater. **192**, 203 (1999).

[79] C.-J. Chen, R.-K. Chiang, H.-Yi. Lai, and C.-R. Lin, J. Phys. Chem. C **114**, 4258 (2010).

[80] A. Lak, M. Kraken, F. Ludwig, A. Kornowski, D. Eberbeck, S. Sievers, F. J. Litterst, H. Weller, and M. Schilling, Nanoscale **5**, 12286 (2013).

[81] D. Wilson, M. A. Langell, Appl. Surf. Sci. **303**, 6 (2014).

[82] D. Matthey, J. G. Wang, S. Wendt, J. Matthiesen, R. Schaub, E. Lgsgaard, B. Hammer, F. Besenbacher, Science **315**, 1692 (2007).

[83] X. Teng, M. Feygenson, Q. Wang, J. He, W. Du, A. I. Frenkel, W. Han, and M. Aronson, Nano Lett. **9**, 3177 (2009).

[84] C. W. Mays, J. S. Vermaak, and D. Kuhlmann-Wilsdorf, Surf. Sci. **12**, 134 (1968).

[85] K. Ishikawa and T. Uemori, Phys. Rev. B **60**, 11841 (1999).

[86] G. Li, J. Boerio-Goates, B. F. Woodfield, and L. Li, Appl. Phys. Lett. **85**, 2059 (2004).

[87] V. Perebeinos, S. W. Zhang, and F. Zhang, Solid State Commun. **123**, 295 (2002).

[88] M. Estrader, A. Lopez-Ortega, I. V. Golosovsky, S. Estrade, A. G. Roca, G. Salazar-Alvarez, L. Lopez-Conesa, D. Tobia, E. Winkler, J. D. Ardisson, W. A. A. Macedo, A. Morphis, M. Vasilakaki, K. N. Trohidou, A. Gukasov, I. Mirebeau, O. L. Makarova, R. D. Zysler, F. Peiro, M. Dolors Baro, L. Bergstroem, J. Nogues, Nanoscale **7**, 3002 (2015).

[89] J. Nogués, J. Sort, V. Langlais, V. Skumryev, S. Suriñach, J. S. Muñoz, and M. D. Baró, Phys. Rep. **422**, 65 (2005).

[90] S. E. Inderhees, J. A. Borchers, K. S. Green, M. S. Kim, K. Sun, G. L. Strycker, and M. C. Aronson, Phys. Rev. Lett. **101**, 117202 (2008).

[91] S. Estrade, Ll. Yedra, A. Lopez-Ortega, M. Estrader, G. Salazar-Alvarez, M. D. Baro, J. Nogues, and F. Peiro, Micron **43**, 30 (2012).

[92] Ll. Yedra, E. Xuriguera, M. Estrader, A. Lopez-Ortega, M. D. Baro, J. Nogues, M. Roldan, M. Varela, S. Estrade, and F. Peiro, Microsc. Microanal. **20**, 698 (2014).